Impacts of Urbanization on Atmospheric Circulation and Aerosol Transport in a Coastal Environment Simulated by the WRF-Chem Coupled with Urban Canopy Model

Ganghan Kim[1], Joonlee Lee[1], Myong-In Lee[1,*], and Dongmin Kim[2]

[1]School of Urban and Environmental Engineering, Ulsan, Korea

[2]Physical Oceanography Division, National Oceanic and Atmospheric Administration/Atlantic Oceanographic and Meteorological Laboratory, Miami, Florida, USA

Minor Revision

Atmospheric Environment

31 January 2021

---

*Corresponding author: Prof. Myong-In Lee
Department of Urban and Environmental Engineering
Ulsan National Institute of Science and Technology,
50 UNIST-gil, Ulju-gun, Ulsan 44919, Korea
Email: milee@unist.ac.kr

Highlights

- Urbanization induces thermally-driven atmospheric secondary circulation and affects the dispersion of air pollutants over the populated city.
- Enhanced vertical mixing and vertical transport contribute to decreasing the air pollutant concentration near the surface level both daytime and nighttime over the urban area.
- The thermodynamical impacts of urbanization are more efficient in reducing ground-level air pollutant concentration in the nocturnal stable boundary layer.

Abstract

This study examines the impacts of urbanization on the local atmospheric circulation and the dispersion of air pollutants over the populated city of Ulsan, South Korea, located in the coastal region. Two experiments are conducted using the Weather Research and Forecasting model coupled with Chemistry (WRF-Chem) and the urban canopy model (UCM) at 1-km horizontal resolution. The model experiments are conducted in August for three consecutive years of 2016-2018, with an updated land use category and diurnally-varying surface emission and anthropogenic heat flux. The impacts of urbanization are isolated by comparing the control run (CTRL) with realistic land use conditions and the sensitivity run (NOURB) that replaces the urban surfaces with non-urban grasslands. CTRL reproduces the urban heat island (UHI) and associated wind patterns realistically with reliable local land-sea breeze circulations. The positive temperature anomalies develop over the urban area due to enhanced surface heat flux at the urban surfaces, driving low-level convergence and secondary circulation. Enhanced heating by UHI changes the ground-level aerosol concentration differently. While the concentration does not change significantly by UHI in the daytime, it is reduced considerably at night in the urban areas due to enhanced vertical mixing. The dominant process that the urbanization modifies the aerosol concentration is the thermodynamical effects, which are also supported by the observation.

Keywords: WRF-Chem; urban canopy model; land-sea breeze; urban heat island; aerosol concentration

1. Introduction

Urbanization is becoming one of the crucial issues affecting regional weather and climatic states. Concrete building and asphalt-covered roads change the land surface radiative properties such as surface albedo and emissivity and thermal properties, including heat capacity and thermal conductivity. Limited vegetated areas and less permeability cause a significant reduction of evapotranspiration. Therefore, the urban surfaces exchange energy with the atmosphere mostly through radiation and sensible heat fluxes, driving warmer and drier meteorological environment in the urban area. Another aspect is the dense and complex three-dimensional building structures, particularly in the metropolitan cities. It effectively increases the heat capacity by trapping longwave radiation and the sensible heat fluxes, thereby confining heat within the urban area. This aspect is known as the urban heat island (UHI), as confirmed in the observational data (Morris et al., 2001; Gedzelman et al., 2003; Kim and Baik, 2004; Kim and Baik, 2005; Fujibe, 2011), resulting in a significant thermal difference between urban and rural area. UHI can be further enhanced by increased roughness length and slow-down of surface wind. Moreover, anthropogenic heat from energy use in the residential and industrial regions aggravates the UHI.

In addition, urbanization significantly changes the local atmospheric circulation (Bornstein and Lin, 2000; Arnfield, 2003). Lin et al. (2008) showed that UHI intensity in Taiwan is as high as 4-6 °C, and dry surface induces rapid temperature increase over the city in the morning and produces earlier sea breeze development based on numerical experiments. Other numerical studies also suggested that urban parameter changes impact the urban heating and local circulation change (Kusaka et al., 2001; Holt and Pullen, 2006; Lee et al., 2010).

Other observations- and model-based studies suggest changes in precipitation by urbanization. A couple of studies indicate that urbanization tends to increase precipitation due to enhanced upward motion over urban regions (e.g., Shepherd et al., 2010; Lin et al., 2011;

Wan et al., 2013; Shimadera et al., 2015). An increase in vertical convection over the urban area is also suggested to increase the warm-season precipitation (Fujibe, 2003). In contrast, other model-based studies indicate the reduction of precipitation in the summer season by decreasing evapotranspiration over expanded urban regions (e.g., Zhang et al. 2009).

Many studies highlight the urbanization impacts on thermal comfort, the slow-down of near-surface wind by enhanced momentum mixing, the thermally-driven local circulation, and the possible precipitation changes. However, relatively few studies exist focusing on the urbanization impacts on the regional air pollutant distribution and transport. Although aerosol concentration is generally higher in the urban area due to many anthropogenic pollution sources, it is less acknowledged how urbanization can impact aerosol transport and redistribution through thermal and mechanical circulation changes.

A handful of studies investigated the urbanization impacts on air pollution. For example, ozone concentration in urban areas is enhanced due to increasing temperature and wind speed reduction (Wang et al., 2007, 2009; Jiang et al., 2008). Makar et al. (2010) illustrated that lake-breeze circulation leads to elevated ozone concentration in North America. Ryu et al. (2013) suggested that the low-level advection from surrounding air mass, which has low NOx and high biogenic volatile organic compound (BVOC) concentration, tends to increase ozone production efficiency over an urban area. In contrast, some studies explained that the enhancement of UHI due to the strong turbulence could reduce surface air pollutant concentrations in the urban area (Fallmann et al., 2016).

From the mixed understanding across the previous studies on the role of urbanization on the air pollutant distribution, it can be argued that the urbanization impact on aerosol concentration depends on the meteorological factors (e.g., local circulation, surface air temperature, and cloud formation and precipitation), which are again sensitive to the local geography and the complexity of the terrain. In this regard, more in-depth studies are needed to understand the impacts of urbanization on the modification of local circulation and hence the aerosol distribution. One can speculate the role of urbanization in two aspects: the dynamical and thermodynamical effects. The dynamical effect may reduce the wind speed over urban regions, thereby enhancing air pollution at the surface by limiting horizontal and vertical transport. On the other hand, the thermodynamical effect induced by UHI may reduce surface pollutant concentration through enhancing thermally-driven secondary circulation and upward air pollutant transport. The net effect remains elusive, and carefully-designed model experiments and observational studies can address this scientific question.

This study aims to improve our understanding of the mechanisms of urbanization and its impacts on the atmospheric circulation and the subsequent air pollutant distribution. This study selects the Ulsan Metropolitan City in South Korea as a numerical modeling testbed located right between ocean and mountain regions. Due to these complex geographic features, the city is considerably affected by mountain-valley and land-sea breezes caused by thermal differences. The city also hosts several global industrial companies and national industrial complexes, contributing to various air pollutants. This study uses the community model coupled with the urban canopy model (UCM), which can consider urban surface characteristics in exchanging heat and momentum in the urban canopy area (Kusaka et al., 2001; Holt and Pullen, 2006).

Section 2 provides the model description and experimental designs. Section 3 discusses the results from the model simulation evaluation with the observations and the sensitivity experiments. Lastly, Section 4 provides a summary and further discussion.

2. Model description and experiments

2.1. Model description

This study used the Weather Research and Forecasting model coupled with Chemistry (WRF-Chem) version 3.9.1 (Skamarock et al., 2008; Grell et al., 2005) developed by the

National Center for Atmospheric Research (NCAR). The model has various parameterization options for sub-grid scale meteorological and chemical processes. This study chose the most widely-used schemes, such as the single moment 6-class scheme for cloud microphysics (Hong and Lim, 2006), the rapid radiative transfer model for the longwave radiation (Mlawer et al., 1997), Dudhia scheme for the shortwave radiation (Dudhia, 1989), Mesoscale Model 5 (MM5) similarity scheme in for the surface layer parameterization, Grell-3D scheme for cumulus (Grell and Devenyi, 2002), Noah model for the land surface (Chen and Dudhia, 2001), the Model for Ozone and Related Chemical Tracers (MOZART) for atmospheric chemistry (Brasseur et al., 1998), and the Goddard Chemistry Aerosol Radiation and Transport (GOCART) scheme for aerosol (Chin et al., 2002).

The MOZART chemistry scheme includes a detailed representation of the tropospheric inorganic chemistry mechanisms, small alkane and alkene structures, isoprene, terpenes, and aromatic. The GOCART aerosol schemes simulate 7 different species, including black and organic carbons, sulfate, dust, sea salt, and uncategorized PM_{10} and $PM_{2.5}$. The scheme also divides the species depending on the particle size for dust and sea salt. Five dust bins represent the particles with a radius of 0.5, 1.4, 2.4, 4.5, and 8.0 µm, and four sea salt bins for a radius of 0.3, 1.0, 3.25, and 7.5 µm. Each of the black and organic carbons is divided into two categories of hydrophilic and hydrophobic.

The Noah land surface model is coupled with the UCM over the urban surface to parameterize the UHI mechanisms, in which simplified building and street canyon represent the urban geometry and account for the building shadows and shortwave radiation reflection. The UCM model estimates the surface temperatures of buildings, walls, and roads and their heat fluxes. The urban canopy in WRF is represented vertically either in a single layer (SLUCM; Kusaka et al. 2001) or multiple layers (MLUCM; Martilli et al. 2002, Salamanca et al. 2010). Although the MLUCM parameterization is more sophisticated, it tends to substantially underestimate the UHI intensity in our initial test over the study area, compared with the observational data. This study remains to use SLUCM for more realistic simulations for UHI (See Section 3.2)

The WRF community model has two options for the land use category (LUC) based on two different data sources, one from the United States geological survey (USGS) and the other from the International Geosphere-Biosphere Programme-modified Moderate Resolution Imaging Spectroradiometer (MODIS). In our investigation, the LUC data from USGS and MODIS show notable differences in our modeling domain. In particular, the urban surfaces in Ulsan are overestimated in MODIS compared with those in USGS (not shown). Moreover, both data can not resolve the Taehwa River centered in the city due to its insufficient resolution. Therefore, this study updates the LUC in the model based on the Korea Land Cover (KLC) data produced by Kang et al. (2009). KLC classifies the LUCs into 10 different types based on the leaf area index from the MODIS satellite data, which shows a more realistic spatial distribution of LUCs. This study replaces the urban and built-up land categories in USGS with high-intensity residential areas classified in KLC.

2.2 Model configuration and experiments

Most of the results are based on the numerical model simulations in this study due to sparse observation sites. Figure 1 shows the modeling domain. The main domain D1 covers Korea and a part of Japan at a horizontal resolution of 12 km, and two sub-domains D2 and D3 are successively nested with overlapping at 3 km and 1 km, respectively. This study sets up 30 vertical levels topped at 50 hPa in the hybrid sigma-pressure coordinates. It has a high vertical resolution near the surface, starting from the lowest model level (sigma = 0.998) at approximately 0.128 km from the ground. The initial and boundary conditions for meteorology are specified with the European Centre for Medium-Range Weather Forecasts (ECMWF)

Interim reanalysis (ERA-Interim) data with an original resolution of 80 km. The model is initialized at 12 UTC (09 LST) 31 July and integrated for 31 days until 23 UTC (08 LST) 31 August for three consecutive years of 2016, 2017, and 2018. In detail, each model integration is performed for 84 hours (3.5 days) and then returned to 12 hours before for the next integration for another 84 hours. Initial data for 12 hours are discarded for spin up. This integration method can reduce systematic biases and uncertain model drift (García-Díez et al., 2013).

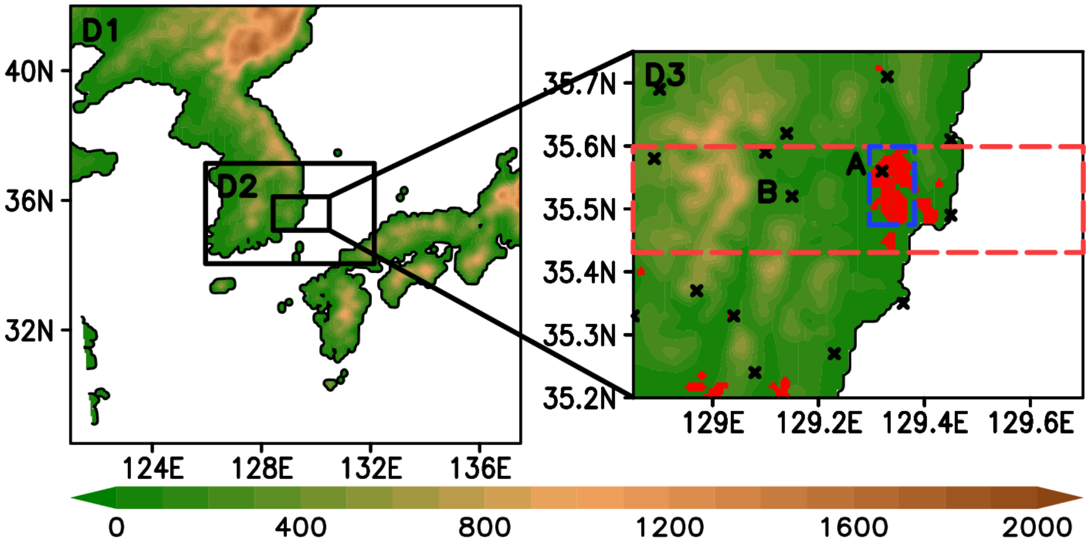

Figure 1. Modeling domains with the main domain D1 at a horizontal resolution of 12 km, the first nested domain D2 at 3 km, and the innermost domain D3 at 1 km. Shaded is the surface elevation (unit: m). The red shaded area in D3 indicates the urban surfaces. The black x-marks indicate the Automatic Weather Stations (AWS). Points A and B are selected as the representatives for the urban and the rural areas for the model verification. The red dashed box indicates the area for the zonal-vertical cross-section with the meridional average, and the red shading in the blue box represents the urban surfaces in Ulsan.

Two numerical experiments are conducted to investigate the impacts of UHI and the changes in air pollutant concentration. CTRL is the experiment with a realistic surface type, and NOURB is the one with the urban surfaces in CTRL replaced with the non-urban grasslands for the red dashed area shown in Fig. 1. As the urban surfaces in Ulsan are originally surrounded by grasslands, this is intended to make the model feel no difference in the surface type over the targeted area. Both experiments share the same model configuration, including initial and boundary conditions, except for the surface type.

The urbanization impacts are reflected in the model experiments by two significant factors. Besides the effects parameterized by the UCM, this study specifies additional anthropogenic heat flux over the urban surfaces. Although the anthropogenic heat sources are diverse, including cooling and heating buildings, manufacturing, transportation, lighting, and the metabolisms by humans and animals, estimating exact heat from these anthropogenic activities seems challenging. A simple approximation is to utilize the total electricity consumption in a specific city. The Korean Statistical Information Service (KOSIS; http://www.kosis.kr) provides the total electricity usage data such as industrial, commercial, residential, general, educational, lightening, etc., on a monthly basis, and the hourly consumption coefficients for each category. The final hourly-varying, anthropogenic heat flux is estimated by integrating total electricity use in August 2018 after multiplying the hourly consumption coefficients to the sectoral usages and dividing by total urban surface area in Ulsan. Figure 2 displays the diurnal variation of anthropogenic heat flux specified to the UCM in this study, peaking in the afternoon with a maximum of 41 W m^{-2} at 15 LST and showing the minimum of 24 W m^{-2} at 04 LST. The estimated anthropogenic heat shows a slight decrease around noon, caused by energy consumption from industrial manufacturing. The time-averaged value is around 33 W m^{-2}, and a comparable value of 38 W m^{-2} is specified in Li et al. (2019) for the highly-dense residential area in Berlin. Note that there is considerable uncertainty in the anthropogenic heat flux estimation, and it may differ depending on the methods. Lee et al. (2019) estimate the anthropogenic heat in the megacity Seoul downtown as high as 130 W m^{-2} in the summertime. Another study by Loupa et al. (2016) provides anthropogenic heat fluxes up to 150 W m^{-2} in the city center of Athens, Greece, in the summertime, with a daily average of 100 W m^{-2}.

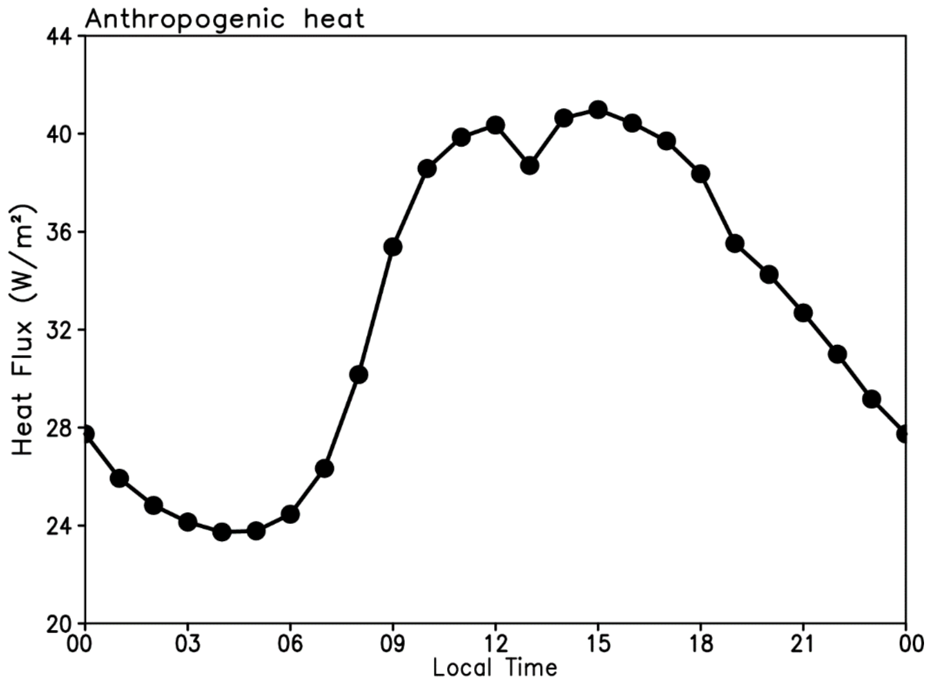

Figure 2. Diurnal variation of anthropogenic heat flux at the urban surfaces, estimated by the Korean Statistical Information Service (KOSIS) total electricity use in August 2018 in Ulsan. See the text for a detailed method.

Another factor that distinguishes the urban surfaces from the non-urban grassland in this study is the surface roughness length. This study specifies 0.75 m for the urban surfaces and 0.11 m for the grasslands, a seven times larger value than the value specified in the grasslands. It effectively decreases the wind speed and influences on the dispersion of air pollutants. From the CTRL configuration, this study carries out another model sensitivity experiment (hereafter CTRL-Z0) to investigate the impacts from the roughness length change by decreasing the value to 0.11 m over the urban surfaces. This experiment is integrated just for five days, sufficient to obtain the sensitivity results (Section 3.3).

The model experiments are commonly forced by the emission data for gas and aerosols inventoried from the Comprehensive Regional Emissions inventory for Atmospheric Transport Experiment (CREATE; Woo et al., 2020). This inventory is the latest one that integrates the local emission inventories from Asian countries in 2015. It uses the Clean Air Policy Support System (CAPSS) national inventory archived for 1999-2011 by the Korean Ministry of

Environment (available at https://airemiss.nier.go.kr/mbshome/mbs/airemiss/index.do). The spatial resolution of CAPSS is 1 km, which supports the resolution of the innermost domain in this study. With the inventories, emission for a specific period is produced by the Sparse Matrix Object Kernel Emission (SMOKE; Benjey et al., 2001) model, driven with the 3-dimensional meteorological data processed by atmospheric models. The CREATE-based emission data provide the diurnal variation based on the local inventory with a pronounced daytime peak in the simulation region (not shown).

This study specifically focuses on the PM_{10} simulation, as it is a lumped mass concentration of 16 aerosols represented by GOCART. It indicates the total aerosol response, and it is ideal for understanding the general impact of urbanization on the air pollutant distribution. The initial evaluation for the simulated PM_{10} concentration significantly underestimates the observed values in Ulsan, presumably due to missing or unspecified emission in the CAPSS data. This study artificially inflates the CREATE-based emission by more than three times, particularly in the daytime, based on the comparison between the simulated and the observed PM_{10} values (see Section 3.2).

2.3 Observation data for model validation

The meteorological data of 2-m air temperature and 10-m wind are obtained from the Korea Meteorological Administration (KMA; available at htttp://data.kma.go.kr) for the official automated surface observing system (ASOS) site and ten automatic weather systems (AWS) sites scattered in Ulsan and its vicinity. The surface PM_{10} concentration data are obtained from the Air Korea website of the Ministry of Environment (available at http://www.airkorea.or.kr) for three stations located in Ulsan. Both datasets cover the same period of model integration (August 2016-2018).

3. Results

3.1 Surface energy balance analysis

Figure 3 compares the diurnal variation of individual heat fluxes between the urban surface and the grassland. By specifying different LUC, several parameters are provided differently over the urban and grassland surfaces. For example, the surface albedo is 0.2 for the urban surface and 0.23 for the grassland, thereby inducing more incoming net downward shortwave radiation at the urban surface. The surface emissivity is specified larger in the urban surface as 0.95, compared with the value of 0.92 at the grassland, suggesting more longwave radiative flux at the urban surface. The urban surface tends to exchange heat with the atmosphere more through sensible heat flux rather than latent heat flux. Comparing with the grassland, the urban surface stores more heat during the daytime and increases the daily maximum temperature. Note that this increased heating during the daytime is balanced by more extended sensible heat and longwave radiative fluxes throughout the evening at the urban surface. At much suppressed latent heat flux at the urban surface, increased heat storage tends to increase the nighttime temperature in the urban surfaces than in the rural. During the nighttime, the net storage term becomes negative due to a much larger sensible heat flux at the urban surfaces than in the grassland. The sensible heat flux in Fig. 3 includes the anthropogenic heat flux. Compared with Fig. 2, the anthropogenic heat contributes to the most sensible heat flux in the nighttime, while it accounts for about 10 % of sensible heat flux in the daytime. This highlights a more dominant role by anthropogenic heat in the nighttime surface energy balance.

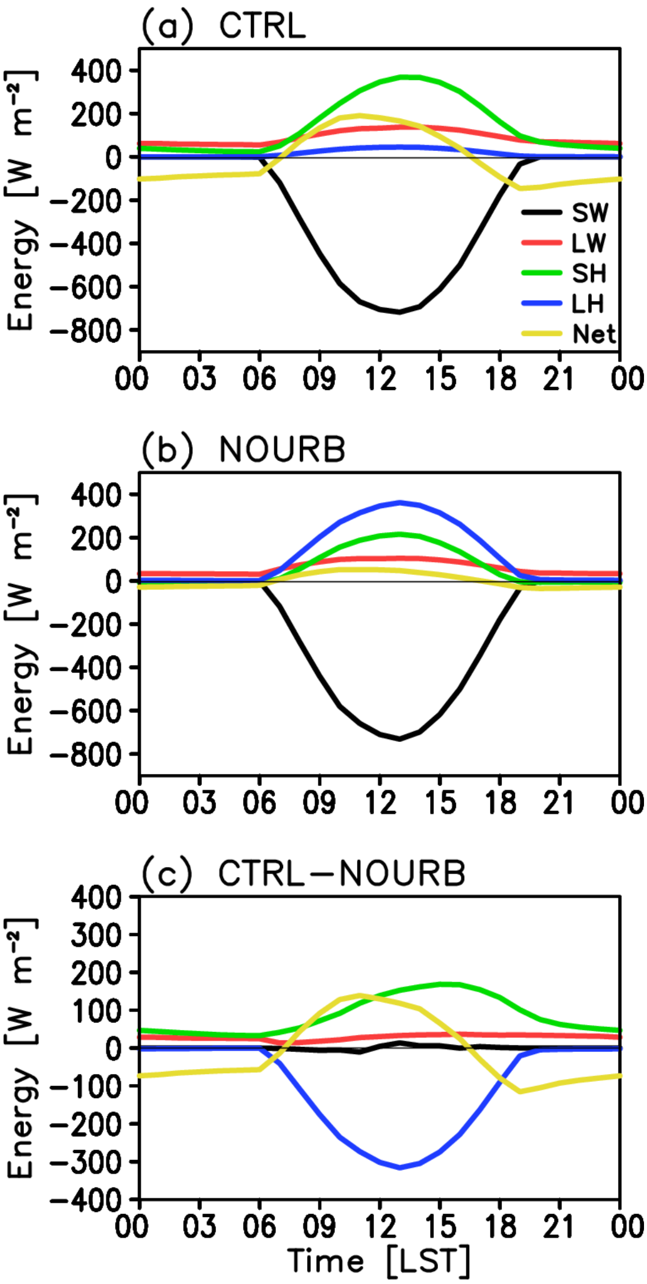

Figure 3. Diurnal variations of the shortwave (black), longwave (red), sensible (green), and latent (blue) fluxes averaged over the urban surfaces (indicated as the red area in the blue box in Fig. 1) (a) and the non-urban surfaces (b). The net heat flux (yellow) indicates the sum of the local storage and ground heat flux. (c) indicates (a) minus (b). The upward flux is defined as positive, and the downward negative in the figure. The unit is W m^{-2}.

3.2 Verification of the model simulation

Figure 4 compares the spatial distribution of time-averaged 2-m air temperature from the observations (Fig. 4a) and the CTRL run (Fig. 4b). The observation data show the temperature of about 26 °C in the city and less than 25 °C in the surrounding regions. Observed temperature shows lower values in the mountain regions located in the west and the north due to high surface elevation. Over this complex terrain, the observational data distribution seems insufficient to resolve the detailed impacts from the surface elevation and heterogeneous surface boundary conditions.

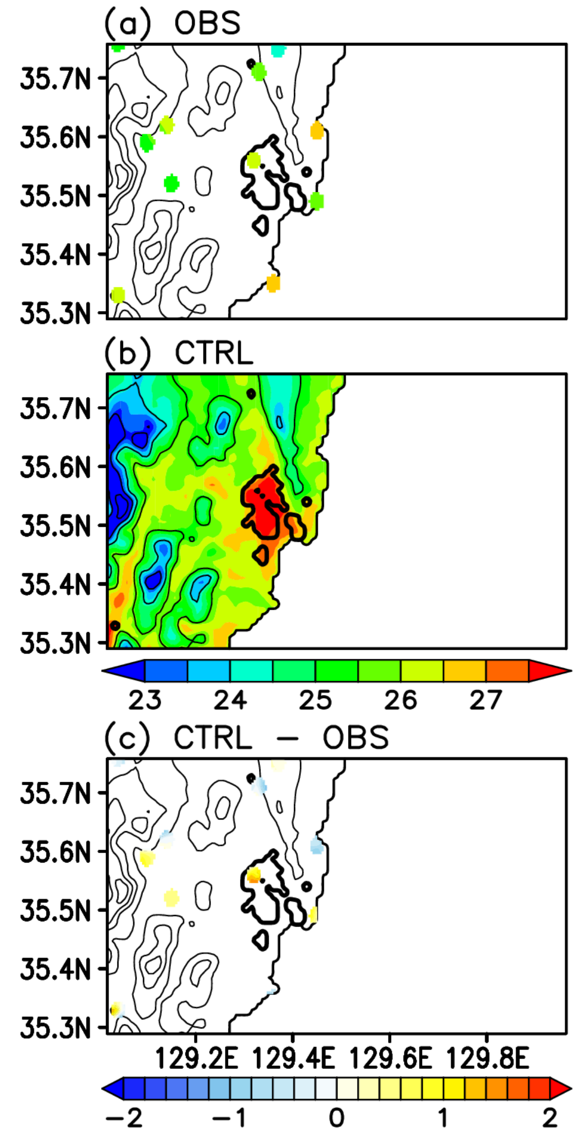

Figure 4. The monthly mean surface 2-m air temperature from (a) the observations (OBS) and (b) the model simulation (CTRL). The contours indicate the height (unit: m) with a 200 m contour interval. The thick black lines indicate the boundary of the urban areas. (c) the model bias (CTRL minus OBS).

The model simulation at 1 km horizontal resolution represents the impacts from the detailed boundary conditions (Fig. 4b). The center of the city and the low elevation regions in the coastal area show relatively high temperatures as in the observations. The spatial pattern of UHI right over the metropolitan city is especially reproduced realistically by the model, although the intensity is somewhat overestimated (Fig. 4c). The simulated temperature over the high mountains has a lot of uncertainty as there exists no observational data for the verification.

Figure 5 examines the consistency between the observed and the simulated temperature over the urban (Site A in Fig. 1) and the rural (Site B) locations for the daily-mean, daytime (12 – 18 LST) and nighttime (00 – 06 LST), respectively. For the daily averages, the observations show higher temperatures in the urban area than in the rural area by the averaged difference of 1.0 °C, indicating the intensity of UHI in the targeted metropolitan city in August. The model simulation tends to reproduce the observed daily-mean UHI intensity but by a difference of 1.5 °C. This is larger than the observation. Overall, the model simulation exhibits a systematic warm bias, particularly in the urban region. When the model bias is considered for the daytime and the nighttime separately, the warm bias in the daily mean temperature is contributed more by the daytime temperature. The bias is almost negligible in the nighttime rural area. The diurnal temperature range in the simulation (observation) is about 4.6 °C (4.3 °C) for urban, and 6.4°C (5.3°C) for rural, respectively. It indicates that the model reproduces the observed larger diurnal variation of temperature in the rural area than in the urban realistically. Despite the systematic UHI bias, the scatter plots from daily samples collected for August in three different years show much resemblance between the observed and the simulated temperature, with correlations between 0.83 and 0.93. This assures that the model reproduces the observed temporal variation in response to various weather conditions.

The smaller diurnal variation in temperature over the urban area is consistent with Georgescu et al. (2012). Urbanization tends to reduce the amplitude of the diurnal temperature range mostly due to the increase in the nighttime temperature induced by UHI. Note that the observed temperature difference between urban and rural is + 0.3 °C (urban minus rural) in the daytime and + 1.3°C in the nighttime, more than four times larger UHI in the night. The model also reproduces these observed features realistically with + 0.5 °C in the daytime and + 2.3°C in the nighttime, respectively, also more than four times larger UHI in the night by the model simulation.

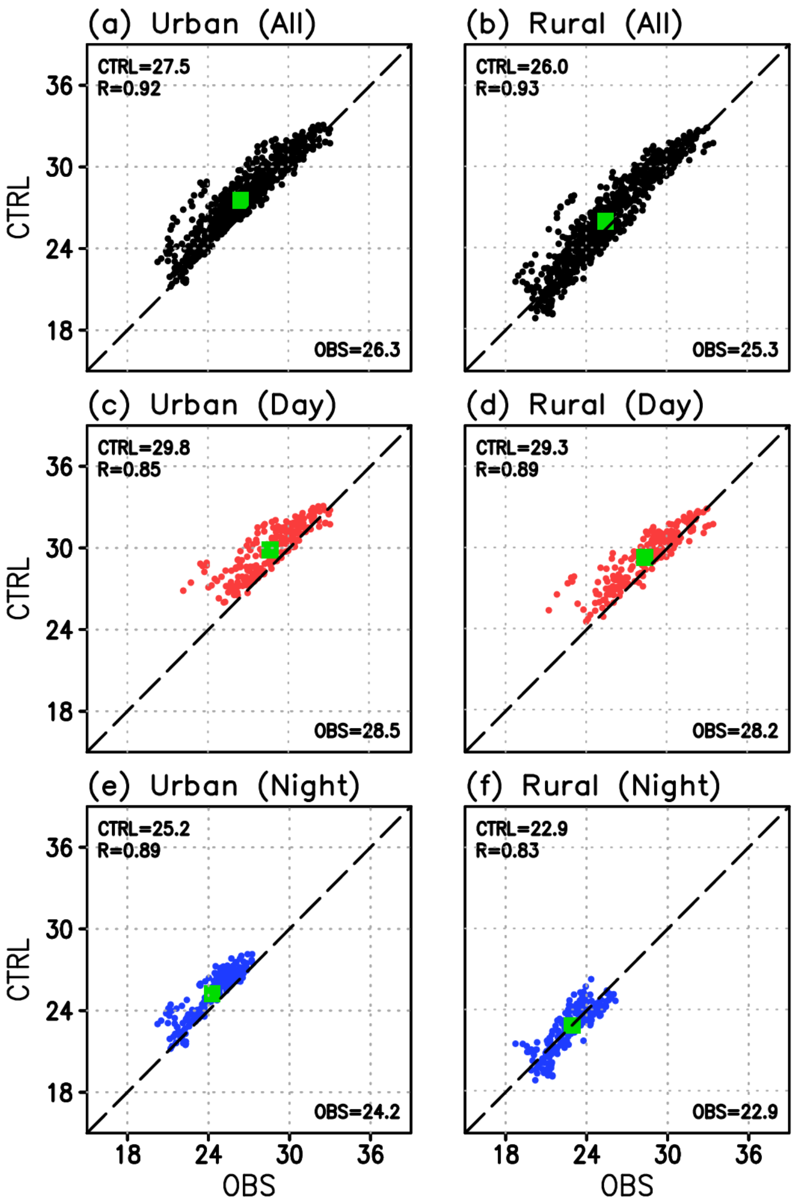

Figure 5. Scatter plots of 2-m temperature between OBS and CTRL over the site A (a, c, and e) and B (b, d, and f) indicated in Fig 1. The black dots (a,b) indicate the temperature distribution throughout the whole day in August 2017-2019. Red (c, d) and blue (e, f) dots denote the temperature distribution during daytime (12-18 LST) and nighttime (00-06 LST), respectively. Each green square of scatter plots presents the average value with the actual value displayed in each panel for OBS and CTRL.

This study further compares the time-mean diurnal variation of 2-m temperature and 10-m wind anomalies over the urban and the rural areas, as illustrated in Fig. 6. In the observed temperature anomalies (Fig. 6a), the diurnal cycle amplitude is weaker in the urban area, as indicated in Fig. 5. The model realistically captures this feature. However, the simulation shows the diurnal peak at 15 LST in the urban area, a 2 hours delay compared with the observational peak at 13 LST. The model performs better in the rural areas in terms of the daily maximum (15 LST) and the minimum (07 LST) temperatures.

The diurnal variation of surface wind anomalies (Fig. 6b) is also quite realistic in the model simulation, even though the wind speed anomalies in CTRL tend to be slightly overestimated in the urban area. This overestimation seems partly related to the prescribed surface roughness length in this study, although the exact estimate of this parameter is unknown. It must be chosen carefully by reflecting local urban geometry characteristics for the targeted area in a future study.

In both observation and simulation, easterly and westerly winds are predominant during the daytime and nighttime. It indicates a typical land-sea breeze circulation with the oceans located in the east of the urban city. The wind bias seems closely related to the temperature variation. Compared to the observation, the model simulation over the urban region maintains a southeasterly sea breeze even longer than observed until evening, somehow consistent with the time delay in the temperature simulations.

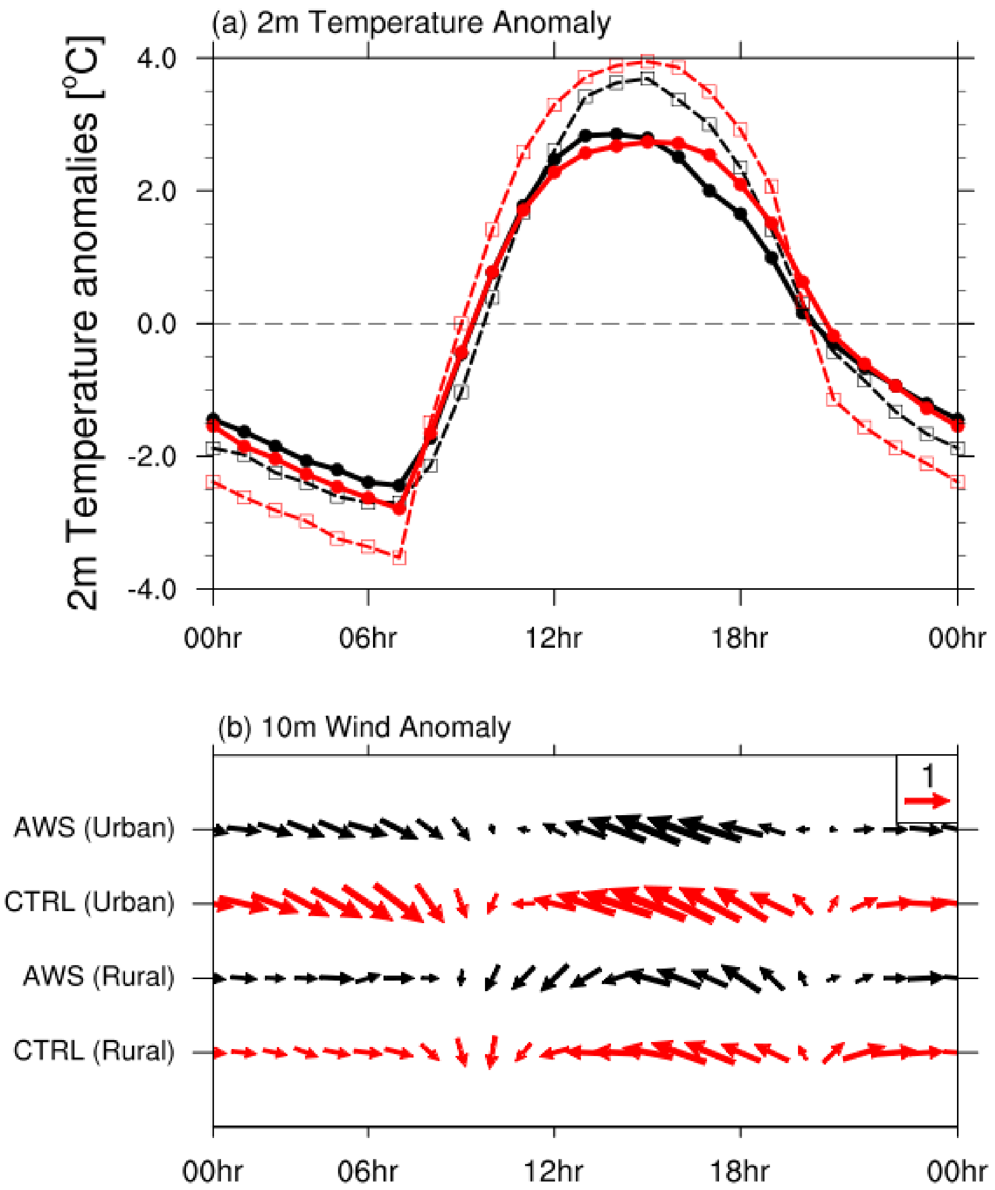

Figure 6. Diurnal cycle of the observed (black) and the simulated (red) 2-m temperature anomaly (a) and the 10-m wind vector anomalies (b). Solid and dashed lines indicate the results of the urban and rural stations, respectively.

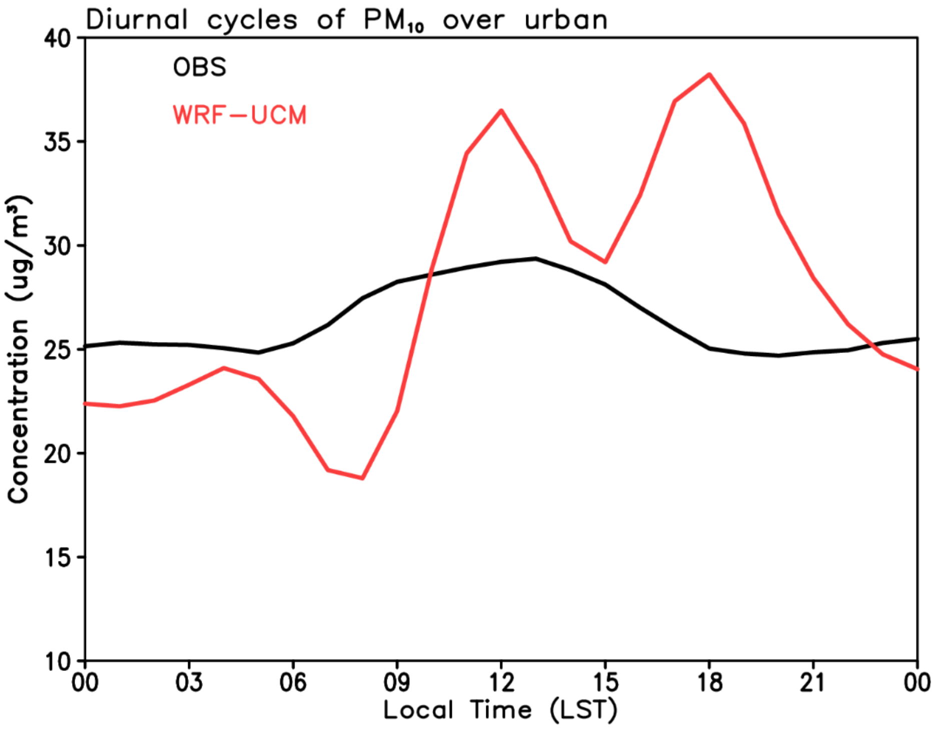

Figure 7. Diurnal variation of surface PM_{10} concentration from the observations (black) and the CTRL model simulations (red). The observations indicate the average of two stations located in the downtown urban region, and the model simulations show the areal average over the observation stations.

This study next verifies the simulated PM_{10} concentration from CTRL with the observations (Fig. 7). Note that the observed concentration is represented by the average of only two urban stations located in the downtown of the city. Considering a large variation of air pollutant concentration in time and space, the comparison is subject to much uncertainty. More observation sites available in the future will facilitate a more quantitative comparison. The observed PM_{10} concentration shows the daytime maximum and nighttime minimum, consistent with the diurnal variation of local emission peaked in the early afternoon in CREATE (not shown). Although the model overestimates the observed diurnal amplitude, it simulates higher PM_{10} concentration in the daytime (12-18 LST) than in the nighttime (00-06 LST) as in the observed. Although the observed values exhibit a single peak, the model shows several peaks at noon (12 LST), evening (18 LST), and early morning (04 LST). The reason for the multiple peaks in the model simulation is not clearly understood. It is just speculated that the model simulation is more prone to the local sea-breeze circulation and air pollutant transport.

Even though CTRL results show a couple of systematic biases in surface temperature and wind (e.g., higher temperatures and stronger diurnal wind diurnal variations over the land surfaces), the simulated UHI and the local land-sea breeze circulation are realistic in reproducing essential features. The diurnal variation of air pollutants is also represented more or less reasonably with the daytime maximum and the nighttime minimum. This assures the qualitative assessment of the impacts of UHI on the local atmospheric circulation and air pollutant transport based on the model sensitivity runs, which is discussed in detail in the next.

3.3 Urbanization impacts on the local circulation

Figures 8a and 8b show the monthly-averaged 2-m surface air temperature distributions with 10-m wind vectors during daytime and nighttime. The thermal contrast between the land and ocean is overwhelming during the day, thereby developing an easterly sea breeze toward the land. As combined with the prevailing wind, the entire domain shows the easterlies. The surface air temperature over the urban area in CTRL is higher than that in NOURB by 0.3 ℃ on average due to the difference in radiative and thermal surface properties between the urban and the grassland types (Fig. 8c). Interestingly, the anomalously warm temperature region is not precisely located over the urban surfaces but shifted to the west in the region of low-level wind convergence, presumably induced by anomalous heating. When the easterlies prevail and pass over the urban surfaces, the wind slows down due to the thermally-driven turbulences and produces a convergence zone on the downstream side.

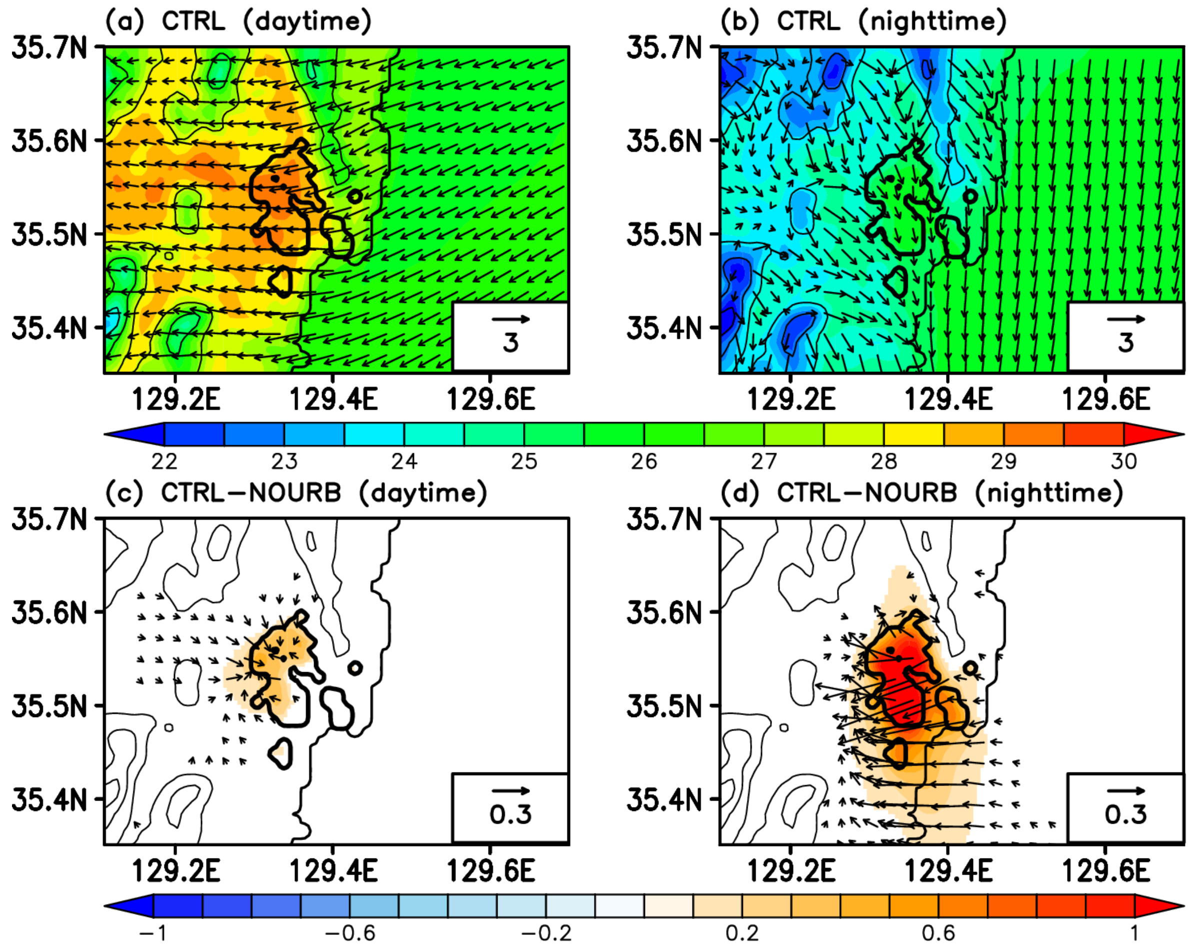

Figure 8 Monthly-averaged 2-m temperature (℃, shaded) and the 10-m wind vectors (m s^{-1}) simulated by CTRL during daytime (12-18 LST) and nighttime (00-06 LST) (a, b). The contour lines indicate height (m, the interval is 200 m). (c, d) the difference (CTRL minus NOURB) during daytime and nighttime, respectively.

In the nighttime (Fig. 8b), northerlies and northwesterlies tend to develop by the land breeze. The temperature over the land becomes colder than that over the ocean due to the nocturnal radiative cooling in the land. Cold mountain wind is also produced on the left side of the urban area due to the nighttime cooling in the high mountainous regions. When these winds are combined with the prevailing wind, the land breeze strengthens the northwesterlies over the land (Fig. 5b).

During the nighttime, the simulated difference in the surface temperature induced by UHI is more than 0.7 ℃ on average in the urban area, which magnitude is larger than that in the daytime (Fig. 8d). Wind difference between the two experiments indicates anomalous low-level easterlies over the urban surfaces, much stronger than those in the daytime. This is driven by the weakening of the land breeze circulation toward the ocean when it passes over the urban surfaces and deflects southward by the anomalous wind convergence by UHI. The heated region by UHI expands in the larger area beyond the border of the urban surfaces. The wind convergence caused by UHI becomes stronger in the nighttime, and the convergence zone is shifted further to the west.

The simulation differences between CTRL and NOURB suggest that the UHI should induce anomalous surface temperature increase and low-level wind convergence. These impacts are isolated well by numerical experiments with differing land surface covers. Except in the vicinity of the urban areas, the differences in temperature and wind between the two experiments are negligibly small for the rest of the simulation domain during daytime and nighttime.

This study further examines the secondary circulation driven by UHI. Figures 9a and b show the vertical cross-section of temperature and wind vectors simulated by CTRL in daytime and nighttime. The simulation domain is featured by a sharp zonal gradient in surface elevation. High mountains in the west area as high as 600 m above the sea level, and the ocean is located in the east. The wind vectors are relatively flat over the sea due to less friction, and they vary up and down over the land due to the complex topography. During the daytime (Fig. 9a), heating over the land area induces the easterly sea breeze in the low level blowing across the domain, and it combines with the valley wind sloping up to the mountains. The wind turns eastward toward the ocean above the 1 km level. Upward motion develops most over the land area, particularly strong at the mountain regions, while the sinking motion dominates over the ocean. The vertical cross-section of wind fields reveals the thermally-driven local atmospheric circulation. In the nighttime (Fig. 9b), the low-level wind over land turns eastward. It is much weaker in magnitude than its counterpart of the daytime sea breeze. The notable difference is over the mountains featured by a downward motion, and the associated downsloping wind is combined with the land breeze in the nighttime toward the ocean.

In a close look, there is another strong vertical motion developing over the urban surfaces in the CTRL simulation both in the daytime and the nighttime, which is better illustrated by the difference map between CTRL and NOURB (Fig. 9c and d). During the daytime over the urban region (Fig. 9c), the temperature contrast between CTRL and NOURB shows the positive anomalies with a maximum at the surface and slightly tilted westward in the vertical direction. This anomalous temperature should be driven by enhanced heat flux from the urban surfaces and reaches the 800 m level. Anomalous heating drives a strong upward motion at the center of the urban area, reaching as high as 2 km level. Compensating downward motion appears in the west of the heating region in the aloft, accompanied by the mass-conserving horizontal motion toward the urban area. In the nighttime (Fig. 9d), positive temperature anomalies over the urban area become stronger and confined within the lowest hundred meters. This feature contrasts with the daytime temperature anomalies stretching in vertical up to 800 m. Suppressed vertical motion in the nighttime background flow and the turbulence suppression at the stable boundary layer is responsible for weak upward heat transport, which aggravates the UHI near the nighttime ground level. The upward motion over the urban area slopes eastward, and the compensating downward motion appears in the east of the heating region. It combines with the anomalously strong low-level easterlies over the urban area and the west.

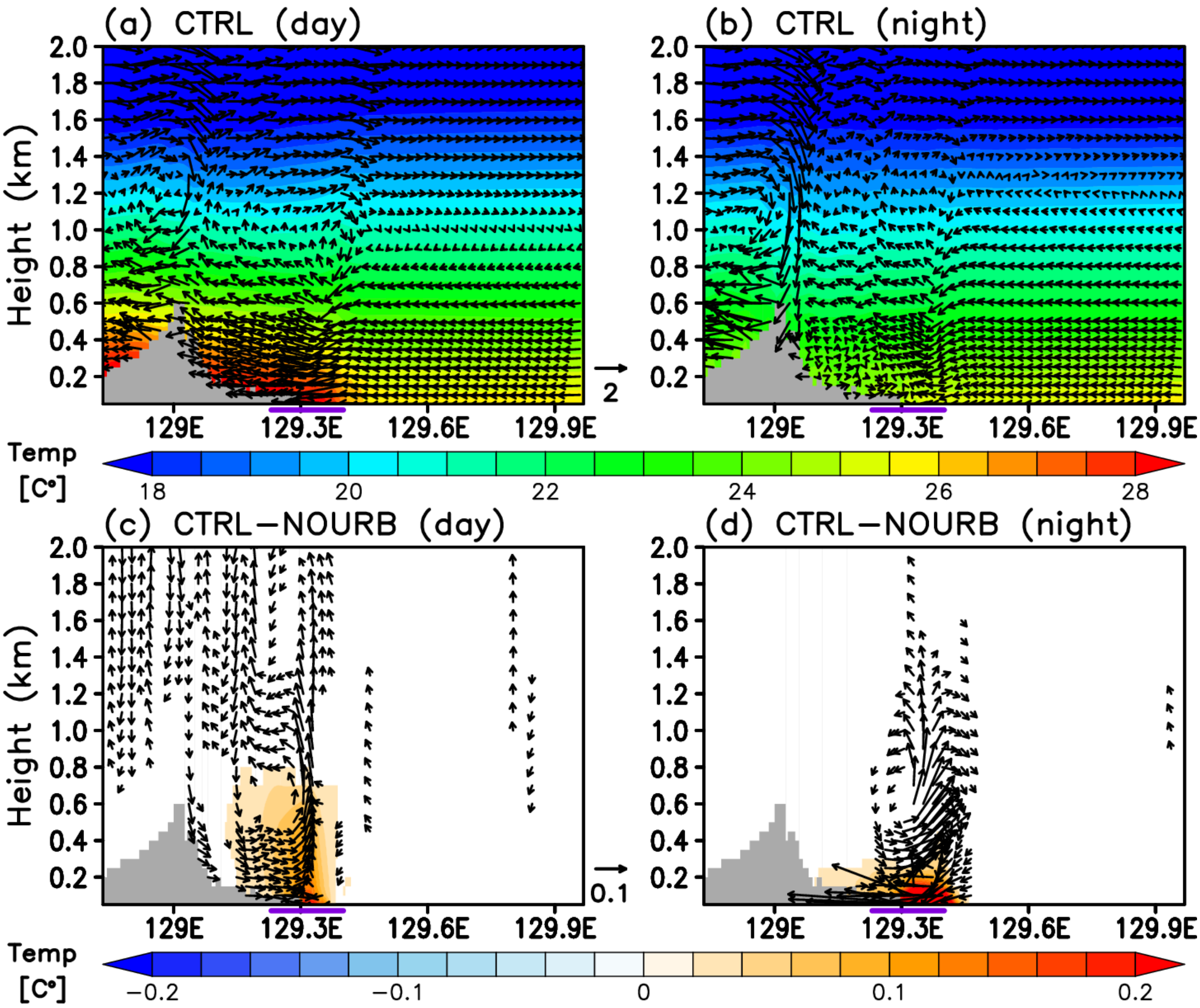

Figure 9 Time-averaged vertical cross-section of temperature (°C, shaded) and wind vector (m s^{-1}) simulated by CTRL over the red dashed box region defined in Fig. 1 during the daytime (12-18 LST) (a) and the nighttime (00-06 LST) (b). (c) and (d) indicates the differences (CTRL minus NOURB). The purple bars in the bottom show the location of the urban surfaces (129.2°-129.4°E).

3.4 Dispersion of air pollutants by urbanization

This study further investigates the impacts on the air pollutant distribution induced by urbanization. Overall, high PM_{10} concentration is simulated near the surface in CTRL, and it decreases in the upward direction due to the emission source at the ground. This tendency is evident when comparing the concentration between the surface and the 300 m level (Figures 10a-d). The PM_{10} distribution patterns also indicate the local land-sea breeze circulation influences, more evident at the 300 m level. The daytime sea breeze passes over the urban surfaces and transports the air pollutants toward the inland region. When the land breeze develops at night, the concentration in the inland region decreases.

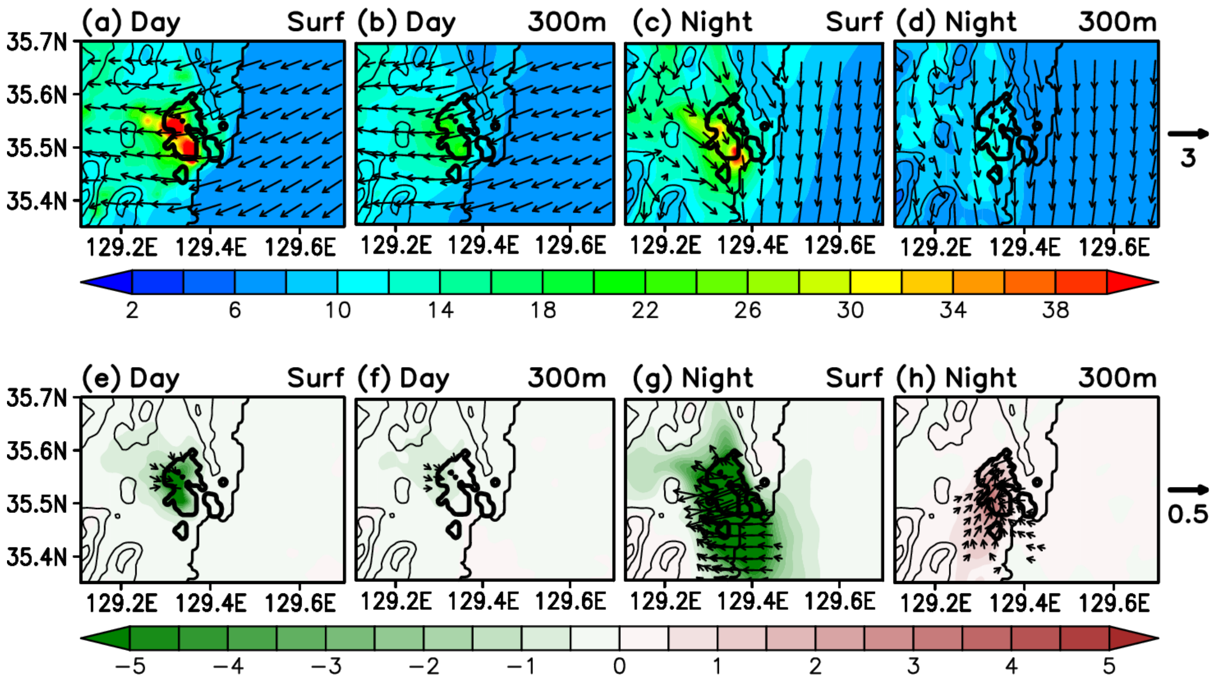

Figure 10 Time-averaged PM_{10} concentration ($\mu g\ m^{-3}$, shaded) and the wind vectors ($m\ s^{-1}$) in CTRL during the daytime (12-18 LST) near the surface (a) and the 300 m level (b). (c-d) are for the nighttime (00-06 LST). The contour lines indicate the surface elevation (m, the interval is 200 m). (e-h) are the same as (a-d) except for CTRL minus NOURB.

In the daytime (Fig. 10e and f), the PM_{10} concentration decreases over the urban areas both at the surface and the 300 m level. The surface concentration level reduces by 15 % on average. Considering that the temperature of the urban areas is relatively higher than that of the rural areas (Fig. 8a), this should result in more enhanced vertical mixing and upward transport of air pollutants. In the nighttime (Fig. 10g and h), the surface PM_{10} reduction is even larger by 73 %. It is found that high temperature in the urban areas in the nighttime tends to perturb the nocturnal stable boundary layer and enhance vertical mixing (Fig. 10g). On the contrary, the concentration of the urban areas at the 300 m level shows the increasing tendency by the introduction of the urban surfaces (Fig. 10h). This suggests that the air pollutant concentration could decrease at the surface but increase in the upper level just below the mixing height. Here the mixing height is distinguished from the mixing layer height, and it denotes the depth of vertical transport and mixing of aerosols. When the mixing height is contracted below the 300 m level by the nocturnal stable boundary layer, air pollutant vertical dilution is limited in the nighttime (Fig. 10h).

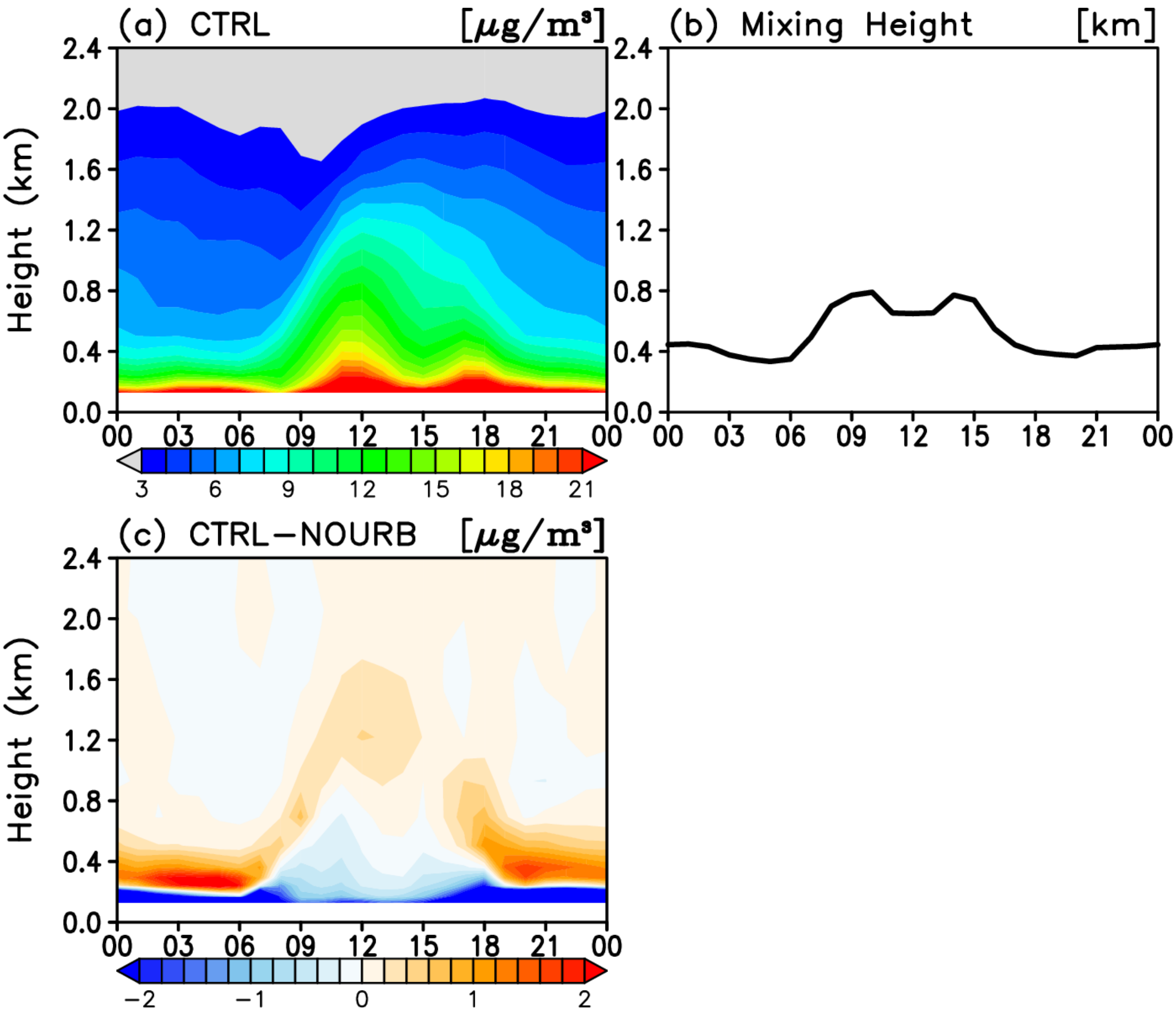

Figure 11 Diurnal variation of the PM_{10} concentration ($\mu g\ m^{-3}$, shaded) averaged over the urban surfaces (indicated as the red area in the blue box in Fig. 1) as a function of height (a) and the diurnal variation of the e-folding height of PM_{10} concentration (b) from the CTRL run. (c) shows the CTRL minus NOURB difference in the PM_{10} concentration. The values in each figure start from the lowest model level at approximately 0.128 km.

This study examines the vertical distribution of the diurnal cycle of PM_{10} averaged over the urban surfaces (Fig. 11a) to understand the asymmetric response in the air pollutant distribution to the UHI between the daytime and the nighttime. In the day, surface heating invigorates the upward motion and turbulence, and the air pollutant is actively transported in a vertical direction and well-mixed with height. On the other hand, vertical aerosol mixing is relatively suppressed in the presence of a stable nocturnal boundary layer. Figure 11b shows the diurnal variation of the aerosol mixing height, defined as the e-folding height of the surface PM_{10} concentration in this study. It reaches up to 0.8 km in the daytime and shrinks to the minimum level below 0.4 km in the evening based on the CTRL experiment.

The vertical distribution of PM_{10} concentration does not change significantly from CTRL to NOURB in the daytime (Fig. 11c), although the UHI induces additional heating in the boundary layer. This suggests that the vertical aerosol transport is already efficient in the daytime, regardless of the additional UHI heating. From the evening to the morning, the PM_{10} concentration shows negative values near the surface and positive above the 300 m level induced by the UHI heating. The response near the surface is due to the enhanced vertical mixing over the urban region induced by UHI heating in the nighttime. Extended heating at the urban surfaces leads to the upward air pollutant transport and accumulate PM_{10} above the 300 m altitude. The anomalously high concentration above the 300 m level in the night disappears after sunrise when the well-mixed boundary layer develops.

The efficiency of air pollutant vertical mixing is closely linked with the changes in the local atmospheric stability. Figure 12 compares the vertical variation of potential temperature as a measure of the static stability for the dry atmosphere. In the daytime (Fig. 12a), it decreases with altitude from the ground level up to 200 m by surface heating and then increases afterward. Low-level heating reduces the static stability and provides a favorable condition for upward motion and enhanced turbulence mixing. The surface heating becomes weak at night, maintaining a stable nocturnal boundary layer with suppressed vertical motion and less turbulence (Fig. 12b). The stability change from NOURBN to CTRL induced by UHI is not apparent until plotting the difference between the two profiles (Fig. 12c and d). The UHI impact induces the low-level potential temperature increase from the surface to the 1.2 km level above (Fig. 12c), which indicates the decrease of the stability in the daytime. It maintains a more unstable condition by low-level heating induced by UHI. At night, the reduction of stability is confined below the 600 m level (Fig. 12d), responsible for the vertically-limited aerosol transport to the upper levels.

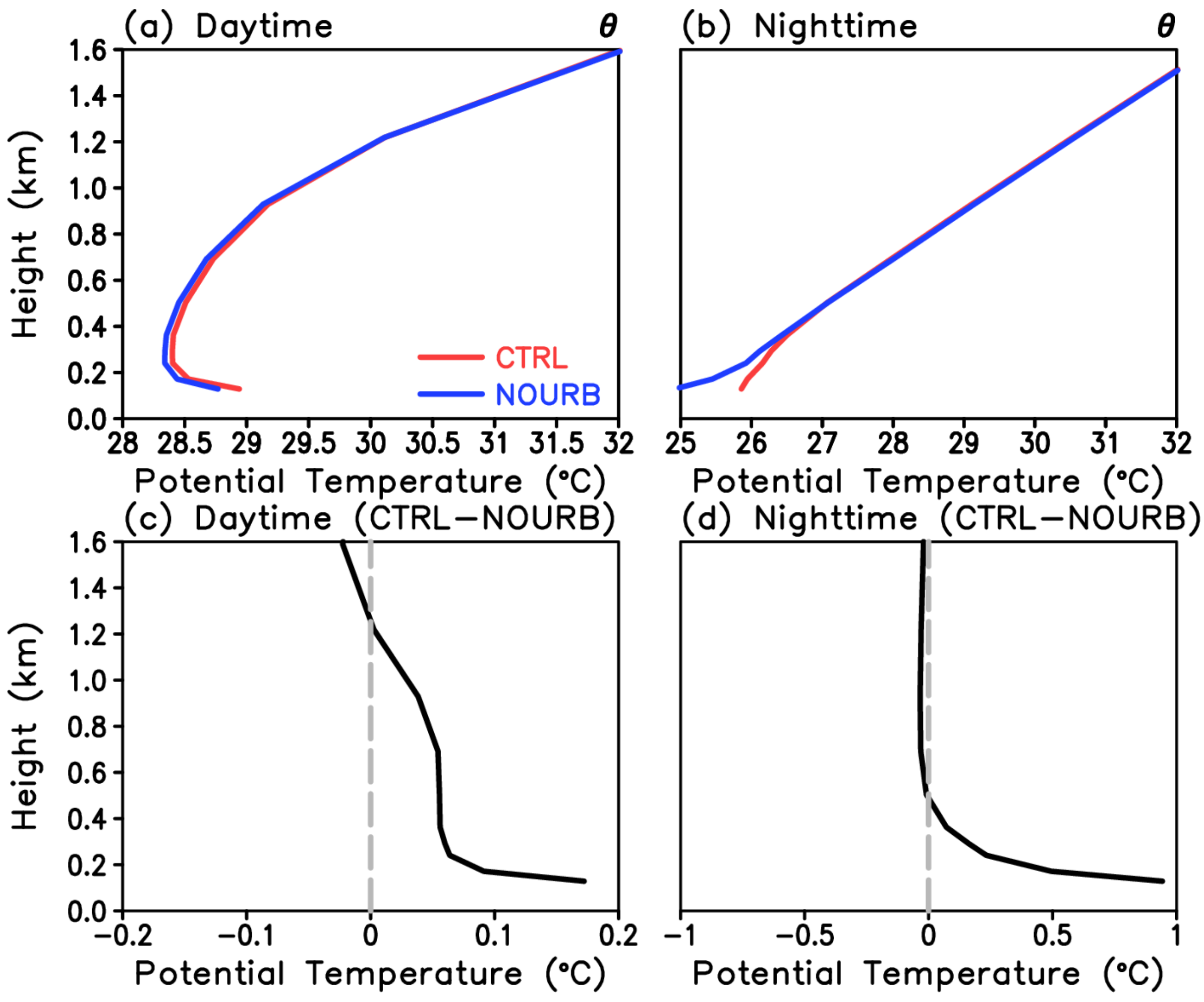

Figure 12 The vertical profile of potential temperature from CTRL and NOURB for the daytime (a) and the nighttime (b), averaged over the urban surfaces. (c-d) are the differences of CTRL minus NOURB for the daytime and the nighttime. The values in each figure start from the lowest model level at approximately 0.128 km.

Processes mentioned above emphasize the critical role of urbanization in the thermodynamical aspect. As mentioned, urbanization generally includes both dynamical and thermodynamical effects, which may operate oppositely in regulating aerosol concentration. The dynamical effects engage the increase of surface roughness length and the decrease of wind speed, which helps accumulate the air pollutant concentration in the urban areas. On the contrary, the thermodynamical effects decrease the air pollutant concentration by enhancing the thermally-driven circulation and upward transport. Various model experiments presented in Fig. 13 confirm these effects. CTRL run with the total urbanization effects reproduces the observed PM10 concentration change between daytime and nighttime reasonably, although the model exaggerates the difference. When the urban surfaces are replaced with non-urban grasslands in NOURB, both the daytime and nighttime concentration increase. This supports the dominant thermodynamical mechanisms caused by UHI. When only the roughness length changes to the non-urban values over the urban surfaces in CTRL-Z0 (i.e., the decrease of surface roughness length), the simulation results are not significantly different from those in CTRL. This suggests the dynamical effect induced by roughness length change plays a relatively minor role in modifying the air pollutant concentration in this model.

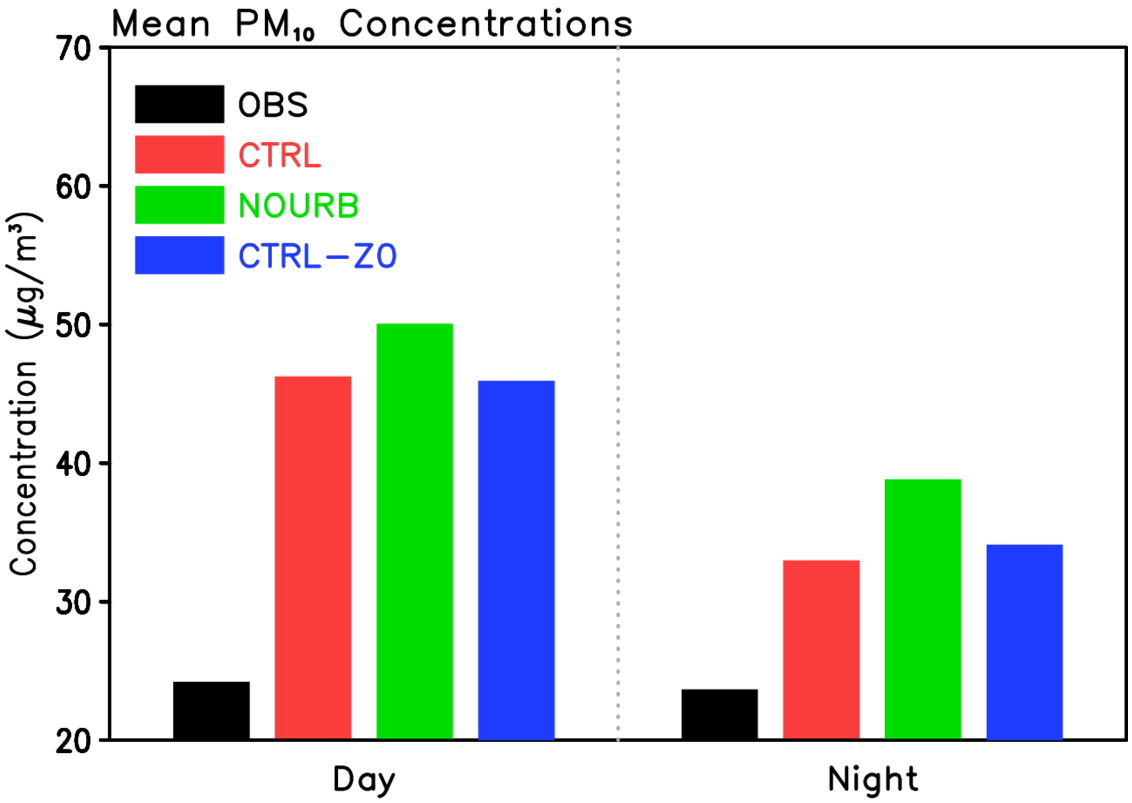

Figure 13 The observed (black) and the simulated PM_{10} concentration from CTRL (red), NOURB (green), and CTRL-Z0 (blue) during daytime (12-18 LST) and nighttime (00-06 LST) over the urban surfaces. Others are the same as in Fig. 7.

Last, this study examines any observational evidence to support the mechanisms suggested by the numerical model simulations in this study. The central hypothesis is the reduced near-ground level air pollutant concentration in the urban region due to more enhanced vertical mixing by UHI in the night. This mechanism is investigated by analyzing the PM_{10} data from two observation sites: one located in the downtown and the other in the suburbs. Figure 14a indicates those sites along with the spatial distribution of PM_{10} emission from CREATE. The downtown site exhibits higher surface emission. Therefore, when the local emission maximizes during a day, the daytime concentration is expected to be higher than that in the suburbs unless the meteorology and aerosol transport are critical. Actual PM_{10} data shows comparable, or even larger value in the suburban station in the daytime (Fig. 14b), implying that the emission does not entirely determine the local air pollutant concentration. Interestingly, nighttime concentration becomes much higher in the suburbs. The substantial reduction in the downtown concentration at night supports the dominant role of thermodynamical mechanisms of UHI in regulating the aerosol concentration near the ground level.

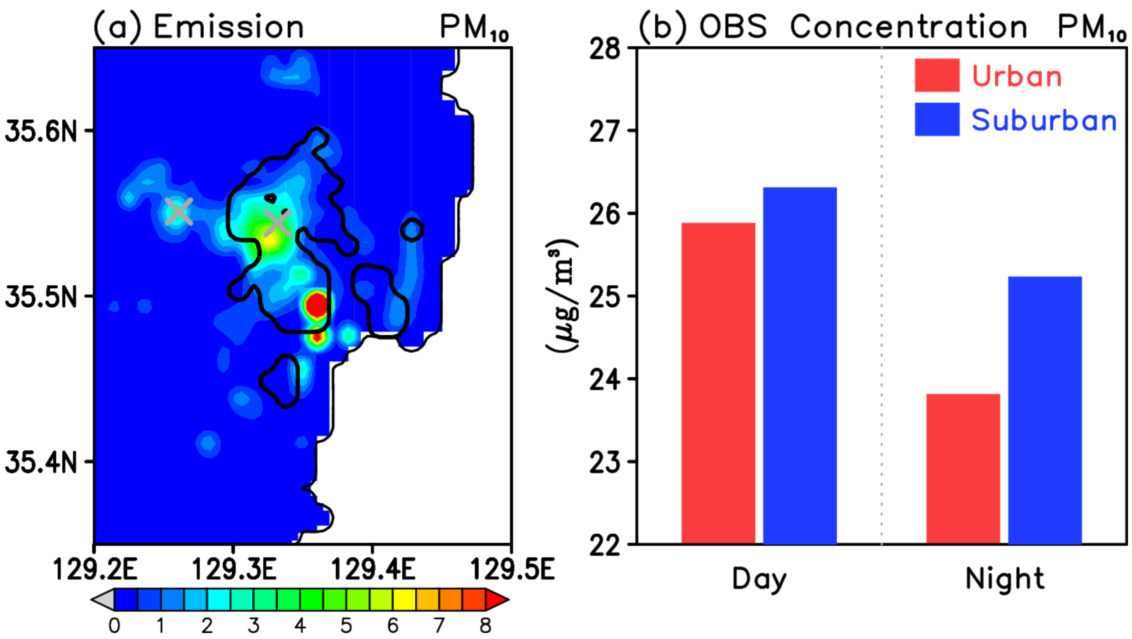

Figure 14 (a) The horizontal distribution of surface PM_{10} emission (unit: $\mu g\ m^{-2}\ s^{-1}$) specified in the model experiments, and (b) the observed PM_{10} concentrations during daytime (12-18 LST) and nighttime (00-06 LST) over the urban and the suburban area. The letter "X" in grey indicates two PM_{10} observation sites located in the urban and suburban regions (inside and outside of the contoured area in black.

4. Summary and Discussion

This study examined the changes in the local atmospheric circulation and the distribution of air pollutants induced by urbanization based on numerical model experiments. Using the single-layer UCM coupled with WRF-Chem at 1 km horizontal resolution, the numerical experiments could evaluate the impacts of urban surfaces. The model experiments were conducted in August for three consecutive years of 2016-2018, driven by a more realistic KLC land use category and the CREATE emission data. Anthropogenic heat flux with a diurnal variation was also applied over the urban surfaces based on the local electricity use.

The control simulation (CTRL) was qualitatively reasonable in terms of representing complex terrain impacts from the mountains and the ocean. The UHI impacts were also reliable in describing the spatial distribution of surface temperature and low-level wind and their diurnal variation compared with the station observations. Another experiment where grasslands intentionally replaced the urban surfaces in CTRL (NOURB) isolated the quantitative impacts of UHI by comparing it with the CTRL run. Both daytime and nighttime, the UHI induces positive 2-m temperature anomalies over the urban surfaces, which leads to low-level horizontal convergence and the enhanced vertical motion. In particular, the temperature difference for the nighttime is larger than that for the daytime, which is related to the suppressed vertical mixing at the presence of the stable nocturnal boundary layer.

Enhanced heating induced by UHI changes the vertical distribution of air pollutants, but with a different response between the daytime and the nighttime. In the daytime, the vertical distribution of air pollutant concentration does not change significantly by UHI. This suggests that the vertical transport of air pollutants is already efficient in the daytime, regardless of the additional UHI heating. At night, the air pollutant concentration over the urban surfaces is reduced, but the concentration at the 300 m or above becomes significantly higher. The response near the surface is due to the enhanced vertical mixing over the urban region induced by UHI. It leads to the upward air pollutant transport and accumulates the air pollutant aloft. Enhanced vertical transport by UHI is attributed to the decrease of atmospheric stability, in which the adjusted layer becomes much shallower and confined near ground level at night.

The thermodynamical effects in urbanization mostly account for the changes in the air pollutant concentration in the model. The dynamical effects tested by the surface roughness length change only do not alter the simulation result drastically. The observation data analysis further examined the modeling mechanisms. The nighttime air pollutant concentration is much lower in the urban regions, despite higher surface emission than in the suburbs. This supports the thermodynamical effects induced by UHI as the dominant mechanism for changing the air pollutant concentration over the urban area.

Our results highlight that the urbanization can dynamically control not only the local circulation but also air pollutant dispersion. From these perspectives, the representation of realistic urbanization in the numerical model is a crucial factor for improving the prediction of the thermal and dynamical features of regional atmospheric states and air quality forecasts. Nevertheless, there are a couple of limitations in this study to move forward in improving our understating of the role of UHI on the local atmospheric circulation and the dispersion of air pollutants. Although we specified the most up-to-date emission inventory from CREATE, this is not ideal for representing local emission due to the old data archived in 1999-2011 and its considerable uncertainty in the diurnal variation of surface emission.

Another aspect of the UHI not considered in this study is its impacts on the redistribution of aerosols in vertical and their interaction and feedback with cloud and precipitation processes. Previous studies suggest that the nocturnal heavy rainfall might be enhanced by increasing cloud seeds (e.g., Huff and Changnon, 1973). Han et al. (2012) also examined that the development of convective cloud under high aerosol concentrations is caused by the release of an increased condensation heating in the strong updraft region due to increasing smaller cloud droplets with high aerosol particles in the clouds. Khain (2009) also suggested that aerosol effects on the cloud system and precipitation due to different environmental conditions. In this regard, future research, including the provision of more detailed local emission data and the test with the interactive aerosol-cloud processes are underway to help improve our understanding of the impacts of urbanization on the local atmospheric circulation change and air pollutant dispersion in the complex terrain.

Acknowledgments

This study was supported by the Basic Science Research Program of the National Research Foundation of Korea (NRF), funded by the Ministry of Education, Science and Technology

(NRF-2018R1A2B6008351)

References

Abdallah C., Sartelet K., Afif C., 2016, Influence of boundary conditions and anthropogenic emission inventories on simulated O_3 and $PM_{2.5}$ concentrations over Lebanon. Atmospheric Pollution Research, 7(6), 971-979.

Arnfield A.J., 2003. Two decades of urban climate research: A review of turbulence, exchanges of energy and water, and the urban heat island, International Journal Climatology, 23, 1–26

Benjey, W., Houyoux, M., Susick, J., 2001, Implementation of the SMOKE emission data processor and SMOKE tool input data processor in Models-3. US EPA.

Bornstein R., Lin Q., 2008. Urban heat islands and summertime convective thunderstorms in Atlanta: three case studies, Atmospheric Environment, 34, 507- 516

Chen F., Dudhia J., 2001: Coupling an advanced land-surface/ hydrology model with the Penn State/ NCAR MM5 modeling system. Part I: Model description and implementation, Monthly Weather Review, 129, 569–585

Dudhia J., 1989, Numerical study of convection observed during the winter monsoon experiment using a mesoscale two-dimensional model, Journal of Atmospheric Science, 46, 3077-3107

Fallmann J., Forkel R., Emeis S., 2016, Secondary effects of urban heat island mitigation measures on air quality. Atmospheric Environment, 125, 199-211.

Fernando H.J.S., Lee S.M., Anderson J., Princevac M., Pardyjak E., Grossman-Clarke S., 2001, Urban fluid mechanics: air circulation and contaminant dispersion in cities. Environmental Fluid Mechanics, 1(1), 107-164.

Fujibe F., 2003, Long-term Surface Wind Changes in the Tokyo Metropolitan Area in the Afternoon of Sunny Days in the Warm Season, Journal of Meteorological Society Japan, 81(1), 141-149

Fujibe F., 2011, Urban warming in Japanese cities and its relation to climate change monitoring, International Journal of Climatology, 31, 162–173, DOI: 10.1002/joc.2142

García-Díez M., Fernández J., Fita L., Yagüe C., 2013, Seasonal dependence of WRF model biases and sensitivity to PBL schemes over Europe. Quarterly Journal of the Royal Meteorological Society, 139(671), 501-514.

Gedzelman S.D., Austin S., Cermak R., Stefano N., Partridge S., Quesenberry S., Robinson D.A., 2003, Mesoscale aspects of the urban heat island around New York City, Theoretical and Applied Climatology, 75, 29–42, DOI 10.1007/s00704-002-0724-2

Georgescu, M., M. Moustaoui, A. Mahalov, and J. Dudhia, 2013: Summer-time climate impacts of projected megapolitan expansion in Arizona. Nature Clim Change 3, 37–41. https://doi.org/10.1038/nclimate1656

Grell, G.A., Dévényi D., 2002, A generalized approach to parameterizing convection combining ensemble and data assimilation techniques. Geophysical Research Letters 29(14), 38-1

Grell G.A., Peckham S.E., McKeen S., Schmitz R., Frost G., Skamarock W.C., Eder B., 2005, Fully coupled "online" chemistry within the WRF model, Atmospheric Environment, 39, 6957–6975

Han J.Y., Baik J.J. Khain A.P., 2012. A numerical study of urban aerosol impacts on clouds and precipitation, Journal of Atmospheric Science, 69, 504-520

Holt T., Pullen J., 2006, Urban Canopy Modeling of the New York City Metropolitan Area: A Comparison and Validation of Single- and Multilayer Parameterizations, Monthly Weather Review, 135, 1906-1930

Hong S.Y., Lim J.O.J., 2006, The WRF single-moment 6-class microphysics scheme (WSM6), Journal of Korean Meteorological Society., 42, 129-151

Huff F.A., Changnon Jr. S.A., 1973, Precipitation modification by major urban areas, Bulletin of the American Meteorological Society, 54, 1220-1232

Jiang X., Wiedinmyer C., Chen F., Yang Z.L., Lo J.C.F., 2008, Predicted impacts of climate and land use change on surface ozone in the Houston, Texas, area, Journal of Geophysical Research, 113, D20312, doi:10.1029/2008JD009820

Kang J.H., Suh M.S., Kwak C.H., 2009, Classification of Land Cover over the Korean Peninsula using MODIS Data, Journal of Korean Meteorological Society, 19(2), 169-182

Khain A.P., 2009, Notes on state-of-the-art investigations of aerosol effects on precipitation: A critical review, Environmental Research Letters, 4(1), 015004, doi:10.1088/1748-9326/4/1/015004

Kim Y.H., Baik J.J., 2004, Daily maximum urban heat island intensity in large cities of Korea, Theoretical and Applied Climatology, 79, 151–164, DOI 10.1007/s00704-004-0070-7

Kim Y.H., Baik J.J., 2005, Spatial and Temporal Structure of the Urban Heat Island in Seoul, Journal of Applied Meteorology, 44,591-605

Kusaka H., Kondo H., Kikegawa Y., Kimura F., 2001, A simple single layer urban canopy model for atmospheric models: comparison with multi-layer and slab models, Boundary-layer Meteorology, 101 ,329–358

Lachatre M., Fortems-Cheiney A., Forêt G., Siour G., Dufour G., Clarisse L., Clerbaux C., Coheur P.-F., Damme M., Beekmann M., 2019, The unintended consequence of SO 2 and NO 2 regulations over China: increase of ammonia levels and impact on PM 2, 5 concentrations, Atmospheric Chemistry and Physics, European Geosciences Union, 2019, 19(10), 6701-6716

Loupa G., Rapsomanikis, S., Trepekli, A., Kourtidis, K., 2016, Energy flux parametrization as an opportunity to get Urban Heat Island insights: The case of Athens, Greece (Thermopolis 2009 Campaign). Sci Total Environ. 542(Pt A), 136-43.

Li H., Zhou Y., Wang X., Zhou X., Zhang H., Sodoudi S. 2019, Quantifying urban heat island intensity and its physical mechanism using WRF/UCM, Science of the Total Environment, 650, 3110-3119

Lin C.Y., Chen W.C., Chang P.L., Sheng Y.F., 2011, Impact of the urban heat island effect on precipitation over a complex geographic environment in northern Taiwan, Journal of Applied Meteorology and Climatology, 50, 339-353

Lin C.Y., Chen W.C., Liu S.C., Liou Y.A., Liu G.R., Lin T.H., 2008, Numerical study of the impact of urbanization on the precipitation over Taiwan, Atmospheric Environment, 42, 2934-2947

Lee H.K., Jee J.B., Yi C.Y., Min J.S., 2017, A Study on High-resolution Numerical Simulation with Detailed Classification of Landuse and Anthropogenic Heat in Seoul Metropolitan area, Korean Journal of Agricultural and Forest Meteorology, 19(4), 232-245

Lee S.H., Baik J.J., 2010, Statistical and dynamical characteristics of the urban heat island intensity in Seoul. Theoretical and Applied Climatology, 100, 227-237

Makar P.A., Zhang J., Gong W., Stroud C., Sills D., Hayden K.L., Brook J., Levy I., Mihele C., Moran M.D., Tarasick D.W., He H., Plummer D., 2010, Mass tracking for chemical analysis: the causes of ozone formation in southern Ontario during BAQS-Met 2007, Atmospheric Chemistry and Physics, 10, 11151-11173, https://doi.org/10.5194/acp-10-11151-2010

Martilli A., Clappier A., Rotach M.W., 2002: An urban surface exchange parameterization for mesoscale models. Boundary-Layer Meteorol 104, 261-304.

Mlawer E.J., Taubman S.J., Brown P.D., Iacono M.J., Clough S.A., 1997, Radiative transfer for inhomogeneous atmosphere: RRTM, a validated correlated-K model for the longwave, Journal of Geophysical Research, 102(D14), 16663-16682

Morris C., Simmonds I., Plummer N., 2001, Quantification of the influences of wind and cloud on the nocturnal urban heat island of a large city, Journal of Applied Meteorology. 40, 169–182

Pernigotti D., Rossa A.M., Ferrario M.E., Sansone M., Benassi A., 2007, Influence of ABL stability on the diurnal cycle of PM10 concentration: illustration of the potential of the new Veneto network of MW-radiometers and SODAR, Meteorologische Zeitschrift, 16(5), 505-511

Ryu Y.H., Baik J.J., Kwak K.H., Kim S., Moon N., 2013, Impacts of urban land-surface forcing on ozone air quality in the Seoul metropolitan area, Atmospheric Chemistry and Physics, 13, 2177–2194, doi:10.5194/acp-13-2177-2013

Salamanca, F., Krpo, A., Martilli, A., & Clappier, A. (2010). A new building energy model coupled with an urban canopy parameterization for urban climate simulations—part I. formulation, verification, and sensitivity analysis of the model. Theoretical and applied climatology, 99(3-4), 331.

Schuch D., Freitas E.D.D., Andrade, M.D.F., 2018, EmissV: A Preprocessor for WRF-Chem Model. Journal of the Atmospheric Science Research, 1(1), online, DOI: 10.30564/jasr.vlil.347

Shepherd J.M., Carter M., Manyin M., Messen D., Burian S., 2010, The impact of urbanization on current and future coastal precipitation: A case study for Houston, Environment and Planning B, 37, 284-304

Shimadera H., Kondo A., Shrestha K.L., Kitaoka K., Inoue Y., 2015, Numerical Evaluation of the Impact of Urbanization on Summertime Precipitation in Osaka, Japan, Advances in Meteorolgy, 2015, 1-11, http://dx.doi.org/10.1155/2015/379361

Skamarock W.C., Klemp J.B., Dudhia J., Gill D.O., Barker D.M., Wang W., Powers J.G., 2008, A description of the Advanced Research WRF version 3. NCAR Tech. Note NCAR/TN-475+STR, 113

Wan H., Zhong Z., Yang X., Li X., 2013, Impact of city belt in Yangtze River Delta in China on a precipitation process in summer: A case study, Atmospheric Research, 125-126, 63-75.

Wang X.M., Chen F., Wu Z.Y., Zhang M.G., Tewari M., Guenther A., Wiedinmyer C., 2009, Impacts of weather conditions modified by urban expansion on surface ozone: Comparison between the Pearl River Delta and Yangtze River Delta regions, Advances in Atmospheric

Science, 26(5), 962-972, doi: 10.1007/s00376- 009-8001-2

Wang X.M., Lin W.S., Yang L.M., Deng R.R. Lin H., 2007, A numerical study of the influences of urban land-use change on ozone distribution over the Pearl River Delta region, China, Tellus Series B, 59, 633–641

Woo, J. H., Kim, Y., Kim, H. K., Choi, K. C., Eum, J. H., Lee, J. B., Lim, J. H., Kim, J. Y., Seong, M., 2020, Development of the CREATE Inventory in Support of Integrated Climate and Air Quality Modeling for Asia. Sustainability, 12(19), 7930.

Zhang C.L., Chen F., Miao S.G., Li Q.C., Xia X.A., Xuan C.Y., 2009, Impacts of urban expansion and future green planting on summer precipitation in the Beijing metropolitan area, Journal of Geophysical Research, 114, D02116, doi:10.1029/2008JD010328